Photonic bandgaps for grating-coupled waveguide modes with a silver tunnel barrier

Z Chen, I R Hooper and J R Sambles[1]

Thin Film Photonics Group, School of Physics, University of Exeter,
Exeter, EX4 4QL, UK
E-mail: j.r.sambles@exeter.ac.uk

Abstract. The optical properties of a periodically modulated photoresist waveguide structure has been explored using the Kretschmann–Raether configuration with a thin silver tunnel barrier. A detailed experimental study of how wavelength-scale periodic texture modifies the dispersion of the guided modes in the visible range for a wide range of azimuthal angles is presented. Fitting the observed in-plane momenta of the modes to predictions from a multilayer, multishape differential grating theory model allows the identities of each of the modes to be confirmed. In addition, the intensities obtained experimentally are compared favourably with those predicted from a theoretical model. Such a waveguide structure can produce not only the photonic bandgaps at the Brillouin zone boundary, but also bandgaps within the Brillouin zone caused by the Bragg scattered guided modes anti-crossing with the unscattered modes. All of these photonic bandgaps have potential applications controlling spontaneous emission in devices.

[1] Author to whom any correspondence should be addressed.

IOP Institute of Physics Φ DEUTSCHE PHYSIKALISCHE GESELLSCHAFT

Contents

1. Introduction

Due to the ability of the interface between a metal and dielectric to support surface plasmon-polaritons (SPPs) [1], structures comprising metal and dielectric layers have been widely studied and used in a number of applications, ranging from sensitive optical probes of metal-film properties [2, 3], surface enhanced Raman spectroscopy [4, 5], biosensors for the detection of biomolecules and bioreactions on a surface [6] to guiding optical waves through metal nanostructures [7]–[10]. The simplest geometry of this structure is that of a planar dielectric layer deposited onto a metal film. In addition to possible excitation of SPPs, such a structure can support guided waves. It is a planar waveguide structure. Hornauer and Raether [11] were two of the first people to record attenuated total reflection (ATR) studies of planar waveguide structures, comprising a 20 μm thick LiF film deposited on a silver tunnel barrier of 50 nm thickness. Through observing the light arising from the scattering of the SPPs by the roughness of the surface, they recorded a series of ATR maxima associated with the excitation of transverse magnetic (TM) and transverse electric (TE) polarized planar guided waves in the LiF layer.

It is well known that the classical grating coupling geometry for SPPs is based on a periodically modulated metal/dielectric interface [12]. More recently, Müller *et al* [13] reported a new kind of grating coupled SPP method, coupling incoming photons via a dielectric grating to a SPP that propagates on a planar metal surface. In their study, a surface-relief grating is introduced into the dielectric film, which was used to successfully couple visible (632.8 nm) radiation to the SPP mode and to study the thermal decomposition of dielectric gratings. Their sample consisted of an evaporated silver substrate, coated with a 5 nm layer of gold and corrugated photoresist grating. This new grating coupling method has also been successfully applied to couple microwave photons to SPPs [14, 15]. A similar geometry is also used by Salakhutdinov *et al* [16] who provided a theoretical and experimental study of increased diffraction efficiency over a conventional metallic grating due to the excitation of leaky modes in the dielectric layer. Other recent studies involving dielectric gratings on flat metal surfaces include that of Yoon *et al* [17]. They reported the efficient outcoupling of the SPPs to transmission modes propagating in free space by use of dielectric diffraction gratings on flat metallic surfaces. Salt *et al* [18, 19] extended such structures by depositing thin cladding metal layers onto the top surface of dielectric gratings/flat metal structures to form asymmetric metallic microcavities. They experimentally and theoretically studied the photonic bandgaps in guided modes of microcavities with transmission measurements at two different azimuthal angles, 0° and 45°. The influence of the one-dimensional (1D) band gap on the 2D dispersion has been demonstrated by comparing the centre frequency and width of the bandgap for two azimuthal angles. The photonic bandgaps produced by such metallic microcavities

can be used to control spontaneous emission by placing the photonic band edge at the emission wavelength [18]–[21]. However, most of these studies are concentrated on the photonic bandgaps at the Brillouin zone boundary. In this study, we investigate the different bandgaps introduced into the dispersion of guided modes by the introduction of the corrugation into the waveguide media.

To more clearly demonstrate how a short-pitch single surface corrugation can modify the dispersion of guided modes, a waveguide structure, simpler in form to that used in the work of Salt *et al* [18], is used: it has no cladding metal layer. The primary simplification is that there is then no SPP mode associated with the upper boundary. Furthermore, the only grating in the structure is an amplitude grating on the dielectric. The structure consists of the waveguide medium, with a periodically modulated upper surface, deposited on an optically thin silver film supported by a silica substrate. The waveguide material is Shipley SPR photoresist which can be easily deposited by spin coating, and can be readily corrugated on its upper surface by developing the pattern produced when the surface is exposed to interfering laser beams. The silver layer, as the tunnel barrier and mirror, should be thick enough to provide a significant reflectivity. However, it should also be thin enough to ensure that there is suitable strength of tunnelling of the evanescent optical field. This thereby allows the guided modes within the photoresist to be studied by observing the reflectivity in the ATR geometry. In addition, in the ATR geometry used, the 1.5 mm thick silica substrate is index-matched to the silica prism to avoid any effect of stray reflection in the substrate.

In this paper, section 2 details the fabrication and structure of the sample. In section 3, the TM polarized reflectivity data of the waveguide structure for the whole range of azimuthal angles in the visible range are presented and analysed in some detail. Firstly, the form of the dispersion curve of the guided modes is obtained from the reflectivity data for each azimuthal angle. In the case of periodically textured surfaces, bandgaps are found due to the presence of counterpropagating modes resulting from Bragg scattering. In addition the reflected intensity as a function of incident optical frequency (ω) for different in-plane momenta (k_{xz}) is computed and compared with the data. Then the optical magnetic field distribution at the resonant frequency for each of the modes is explored to unravel their character. Finally, section 4 provides a brief summary of the work presented.

2. Sample fabrication

The structure used in this study consists of a layer of Shipley SPR700 photoresist on top of a silver tunnel barrier, supported by a flat silica substrate. The fabrication begins with the evaporation of a thin silver film (approximately 60 nm) onto the surface of the silica substrate. The substrate is then spin-coated with photoresist to give a layer approximately 320 nm thick. The thickness is controlled by a choice of concentration of photoresist and spin speed. As is known, in the ATR system, if the metal surface is covered with a dielectric film of higher refractive index than that of the prism the surface plasmon at the metal/dielectric interface may still be excited provided the dielectric film is sufficiently thin [12]. In this case, the thickness of the photoresist is chosen to ensure that the surface plasmon at the silver/photoresist interface will not be excited by direct tunnelling of light from the silica prism. The sample is then baked at 90°C for 30 min to remove the remaining solvent from the resist layer.

To make the grating, the resist is exposed to an interference pattern, using a He–Cd laser operating at a wavelength of 325 nm, followed by chemical developing. Post treatment of the
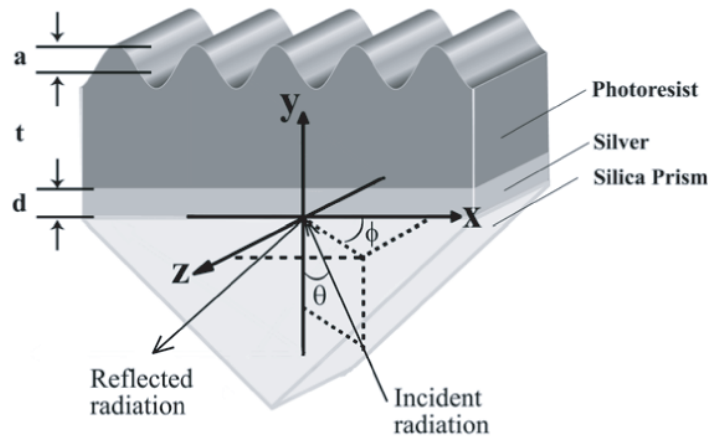
Figure 1. Schematic diagram illustrating the sample, coordinate system, and experimental geometry used in this work. Here, a is the grating amplitude, t is the average thickness of the photoresist layer, d is the thickness of the silver tunnel barrier, θ is the polar angle and ϕ is the azimuthal angle. The silica substrate is optically attached to the silica prism with matching fluid.

resist by thermal baking at 90°C for 30 min and overnight exposure to incoherent UV ensures that the resist is fully stabilized. The pitch, λ_g, of the grating is set at 262.6 nm. A schematic of the sample arrangement, together with the coordinate system used in this paper, is shown in figure 1.

3. Experimental results and discussion

To determine the dispersion of the modes associated with the structure, absolute reflectivity data as a function of wavelength ($400 \leqslant \lambda_0 \leqslant 850$ nm) at different polar angles (θ) and azimuthal angles (ϕ), as defined in figure 1, are obtained as scans in wavelength at various fixed angles. As shown in figure 1, the silica substrate is optically attached to the silica prism with matching fluid to create an ATR system, used for coupling the light into and out of the resist grating structure. The output from a white-light source was spectrally selected using a mono-chromator and this light was then set to TM polarization and made incident on the bottom surface of the silver tunnel barrier through the ATR system. A second polarizer, also set to TM polarisation, is placed directly in front of the detector. When the frequency and in-plane wave vector of the incident light matches a mode in the resist the reflectivity will show a resonant dip. In this way, by measuring the wavelength dependent reflectivity and noting all the reflectivitiy dips, a dispersion diagram is acquired.

In this work, at each azimuthal angle ($0 \leqslant \phi \leqslant 90°$ in steps of 10°) the wavelength dependent absolute reflectivity data was determined for 6 different polar angles ($\theta = 41.6°$, 45°, 48.4°, 51.8°, 55.2° and 58.5°). Figure 2 illustrates just two sets of this reflectivity data, with the polar angle at $\theta = 45°$ and 58.5°, respectively. All of this data is then fitted to models. The modelling used in this paper uses a scattering matrix method based on a conical version of the differential formalism of Chandezon et al [22]. This involves the use of a transformation of coordinates in which the grating surface is essentially flattened allowing easier matching of

the boundary conditions at the corrugated interface. The surface itself is described by a Fourier series:

$$s(x) = a_0 + a_1 \cos(k_g x + \phi_1) + a_2 \cos(2k_g x + \phi_2) + \cdots + a_N \cos(Nk_g x + \phi_N) + \cdots .$$

Here, the a_N coefficient is the Fourier amplitude of the Nth component and ϕ_N is its associated phase shift. From the fitting $a_1 = 35$ nm, $\phi_1 = 90°$, $a_2 = -5$ nm, $\phi_2 = 90°$, $d = 60.8$ nm (the thickness of the silver tunnel barrier, as defined in figure 1), $a_0 = 290.8$ nm (the effective thickness of the photoresist). For the dielectric constants $\varepsilon_{air} = 1$ and $\varepsilon_{quartz} = 2.129$ while $\varepsilon_{resist}(\omega)$ and $\varepsilon_{silver}(\omega)$ are empirically determined by fitting theoretical models to the reflection data and is valid in the visible range[2]. As shown in figure 2, all of the experimental reflectivity data agrees well with theoretical modelling. Also from these reflectivity spectra it is apparent that some reflectivity dips do not change their positions while varying the azimuthal angle (for fixed polar angle) except over a small range of azimuthal angles, in which the reflection dip is interfered with by a Bragg-scattered mode. In figure 2(a), there are two such reflection dips at ~ 425 and ~ 750 nm, respectively. For example at $\phi = 40°$, the reflection dip that should be at ~ 425 nm is significantly red-shifted. In figure 2(b), a similar effect is seen at ~ 565 nm.

Figure 3 shows the model band structure for all the modes (both TM and TE polarisation) supported by the waveguide structure over a certain range of frequency ($f = c/\lambda$) and in-plane wavevector (k_x) at $\phi = 0°$, including the evanescent modes. The two horizontal dashed lines indicate the visible range that can be accessed in the experiments. The dielectric constants stated in (see footnote 2) are only valid in the visible range. In all of the calculations presented here, for those frequencies that exceed the visible range the dielectric constant of silver is modelled as a Drude model with $\omega_p = 1.32 \times 10^{16}$ rad/s and $\tau = 1.45 \times 10^{-14}$ s, while the dielectric constants of the photoresist are fixed to $2.85 + 0.012i$. Clearly, the mode (i) beyond the silica light line is the SPP mode that is supported by the silver/silica interface. We have used the labels TMm and TEm to identify the guided modes, where m is an integer indicating the order of the mode. Mode (ii) is identified as the SPP mode that propagates at the silver/resist interface, the TM_0 mode. Identification of the other modes (iii)–(vi) has been made possible by studying the model reflectivity plots. In figure 4(a), the model TM reflectivity is plotted as a function of frequency and in-plane wavevector for $\phi = 0°$, with the experimental data also being mapped onto this plot: they agree very well. Also plotted are the model TE reflectivities in figure 4(b). The white polygon in the bottom right corner of these plots indicates the inaccessible region beyond the silica light line. By comparing the band structure with the reflectivity plots, it is clear that modes (iv) and (vi) are TM_1 and TM_2 guided modes, and modes (iii) and (v) are TE_1 and TE_2 guided modes, respectively. Figure 3 also demonstrates that all these modes will be 'reflected' at the Brillouin zone boundary. Figure 4(a) clearly shows that both TM_1 and TM_2 modes suffer this Bragg-scattering, and that a bandgap is formed at the first Brillouin zone boundary ($2k_x/k_g = 1$), where the Bragg-scattered mode interferes with the unscattered mode. The experimental data also confirms this Bragg-scattering and the formation of bandgaps. The central frequency of this particular bandgap is g approximately 0.491×10^{15} Hz.

At $\phi = 90°$, the positions of the minima, obtained from the experimental reflection spectra, together with the model TM reflectivity as a function of frequency and in-plane wavevector

[2] $\varepsilon_{resist}(\omega) = -36.69501 + 62.313\omega - 38.187\omega^2 + 11.338\omega^3 - 1.633\omega^4 + 0.091629\omega^5 + i(0.01319 - 8.7131 \times 10^{-16}\omega - 0.0011024\omega^2 - 1.6659 \times 10^{-24}\omega^3 + 9.663 \times 10^{-5}\omega^4 - 1.4567 \times 10^{-18}\omega^5)$,   and $\varepsilon_{silver}(\omega) = -1056.98604 + 1393.3\omega - 754.49\omega^2 + 205.61\omega^3 - 27.963\omega^4 + 1.51149\omega^5 + i(178.76439 - 218.68\omega + 105.182\omega^2 - 24.5992\omega^3 + 2.77223\omega^4 - 0.118922\omega^5)$, where $\omega = 2\pi c/\lambda \times 10^{-15}$ s^{-1}.
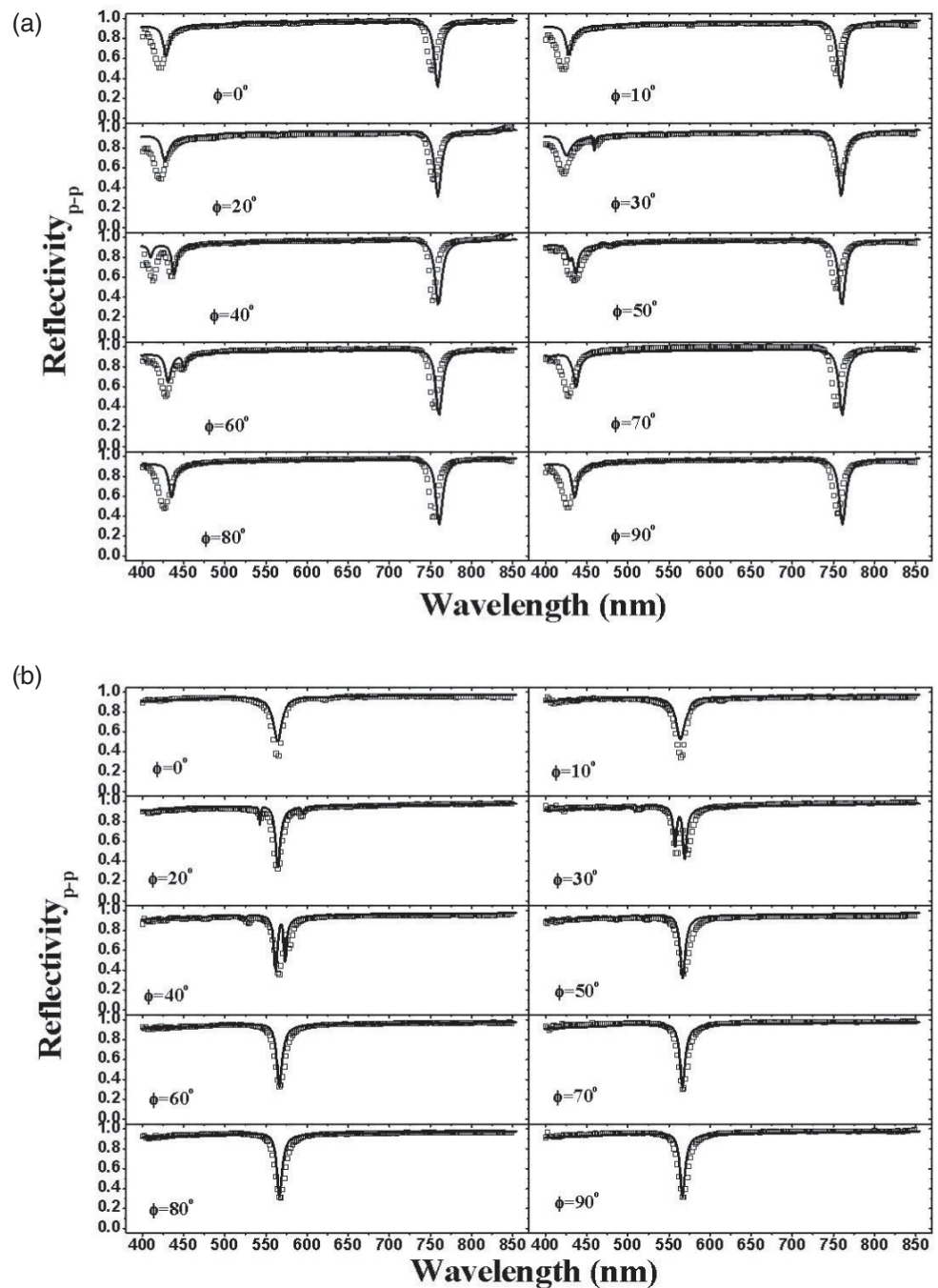
Figure 2. The results of the absolute wavelength-dependent reflectivity for p-polarised incident light at polar angles (a) $\theta = 45°$ and (b) $\theta = 58.5°$. The solid lines on each of the graphs correspond to the theoretically modelled results. The squares are experimental data. The density of experimental data points has been reduced for clarity.
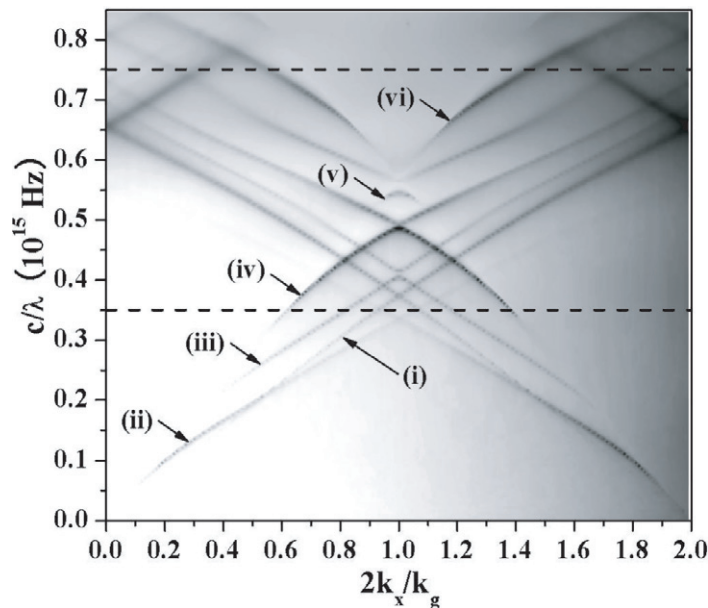
Figure 3. The theoretical band structure for the waveguide structure at $\phi = 0°$. The unscattered modes can be identified as (i) SPP mode that propagates at the silver/silica interface, (ii) the SPP mode that is supported by the silver/resist interface, (iii) TE_1, (iv) TM_1, (v) TE_2 and (vi) TM_2 mode, respectively. All of these modes will occur with Bragg-scattering at the Brillouin zone boundary. The two horizontal dashed lines indicate the visible range that can be accessed in the experiments.

(k_z) are shown in figure 5(a). Also plotted in figure 5(b) is the model TM reflectivity for the planar structure (the top surface of the photoresist is uncorrugated) using the same parameters as described above (the thickness of the resist is taken to be the mean thickness). With TM polarisation at azimuthal angle $\phi = 90°$, the optical electric field is parallel to the grating grooves. In which case we see, by comparing figure 5(a) with (b), that if the modulation of the grating is weak (the amplitude of the grating is small compared to the mean thickness of the photoresist layer), the TM optical response of this system is similar to that of the planar structure. Then comparing the two modes in figure 5(a) with the modes in figure 6, we find that these two modes can be identified as the TM_1 and TM_2 guided modes respectively. Also comparing with the modes in figures 4(a) and 6, we can see that these two modes keep the same positions and profiles when the azimuthal angle is varied from 0° to 90° except over a small range in which they are interfered with by a Bragg-scattered mode. These TM_1 and TM_2 modes are the unscattered TM polarized modes mentioned above.

When the azimuthal angle $\phi \neq 0°$ or $90°$, the dispersion curve becomes more complicated. The major reason for this is that TM polarised light may now excite TE guided modes through the broken symmetry. This will then result in extra corresponding dips in the reflection spectra. These TE guided modes may well be Bragg-scattered and cross with the TM modes. Figure 6 shows the calculated TM reflectivity as a function of frequency and in-plane wavevector (k_{xz}) in the direction of propagation together with experimental data (white squares) for azimuthal angles $\phi = 10°–80°$. At the first Brillouin zone boundary $2k_x/k_g$ should be 1, where the k_x
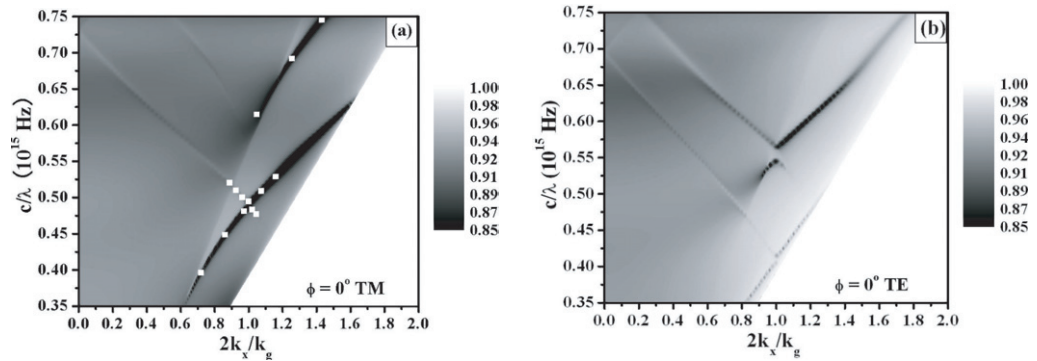
Figure 4. The theoretical TM reflectivity (a) and TE reflectivity (b) as a function of frequency and in-plane wavevector for the waveguide structure with light incident at $\phi = 0°$. The white polygon in the bottom right corner indicates the inaccessible region beyond the silica light line. Two modes, TM_1 and TM_2, can be accessed in the visible range for TM polarisation. The squares in (a) are the mapped reflection dips that are taken from the experimental reflectivity spectra. One bandgap is formed at the first Brillouin zone boundary ($2k_x/k_g = 1$) with the centre frequency $f_c = 0.4912 \times 10^{15}$ Hz.
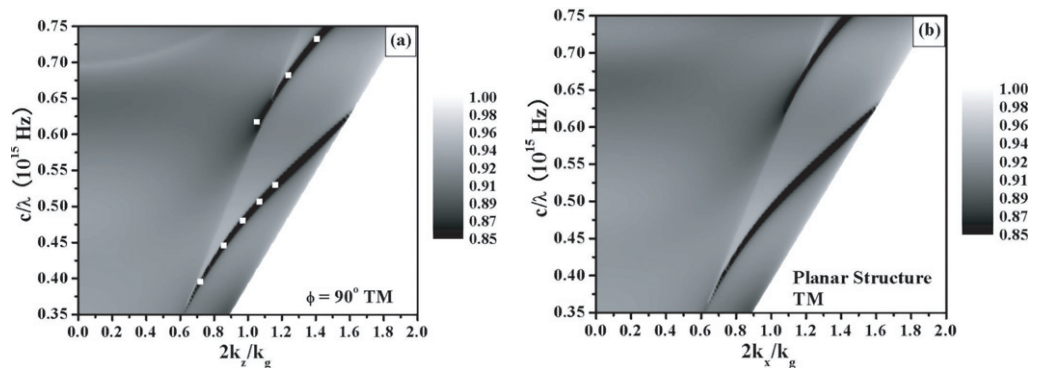

Figure 5. The theoretical TM reflectivity as a function of frequency and in-plane wavevector for the structure with the corrugation on the top surface of photoresist at azimuthal angle $\phi = 90°$ (a), and planar structure without top corrugation (b). The white squares in (a) are the experimental data taken from the reflection spectra. The in-plane momentum k_z and k_x are scaled to $k_g/2$.

component is given by $k_{xz}\cos\phi$. Hence, in these plots, the value of k_{xz} at the first Brillouin zone boundary is given by $1/\cos\phi$. Note that at normal incidence (polar angle $\theta = 0°$) none of the modes vary their resonant frequencies as the azimuthal angle is varied. It is possible to identify the modes found in figure 6, which are marked (i)–(vi), by comparing with the normal incident resonant frequencies of the band structure in figure 3. Modes (i), (ii), (iii) and (iv) are unscattered TM_1 and TM_2, and scattered TM_1 and TM_2 guided modes, respectively. Modes (v) and (vi) are scattered TE_1 and TE_2 modes. In figures 6(a)–(e), the region surrounded by a
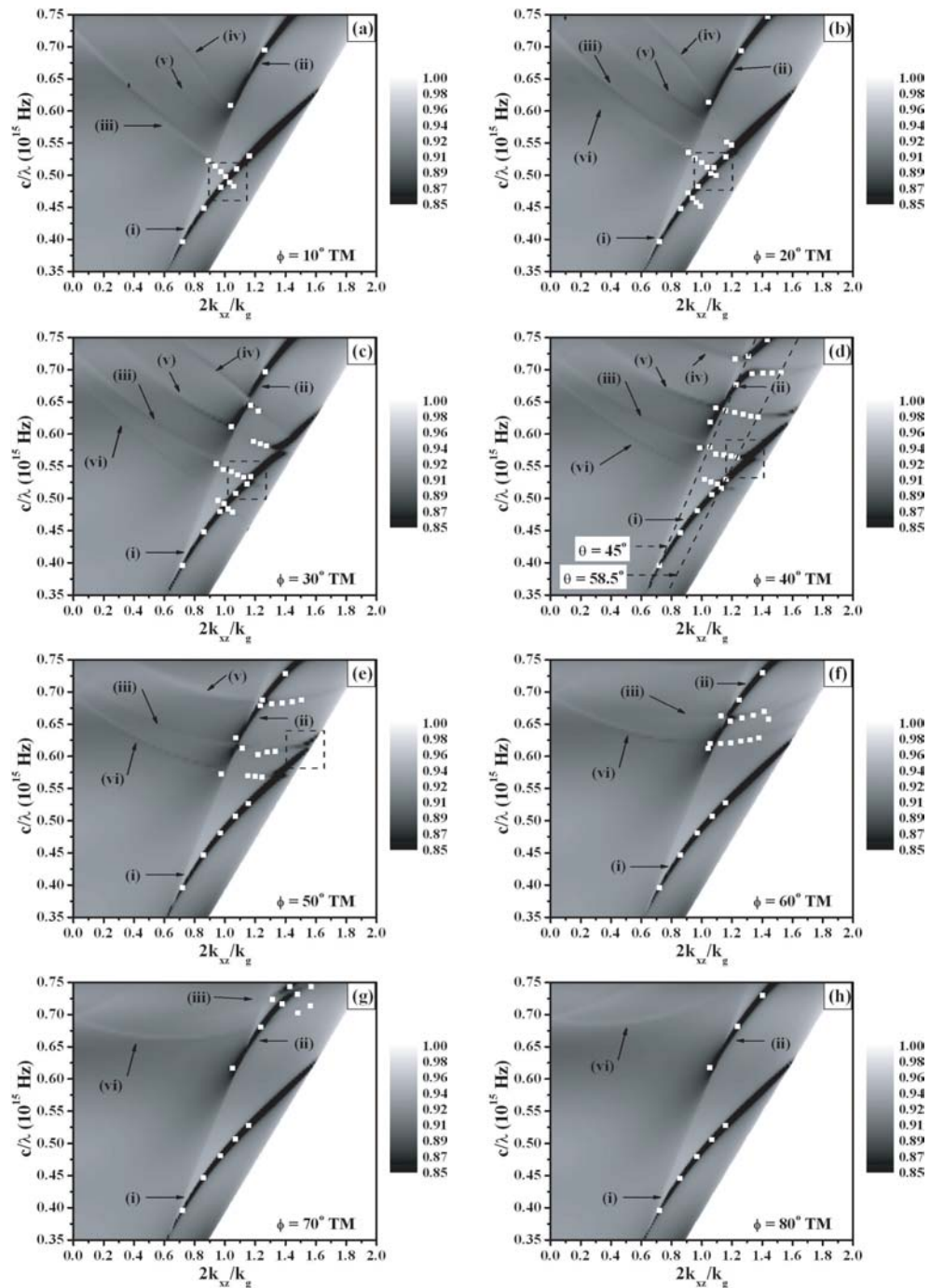
Figure 6. TM reflectivity as a function of frequency and in-plane wavevector for the waveguide structure at $\phi = 10°$–$80°$. The white squares in each plot indicate the corresponding experimental data. The modes marked as (i)–(vi) are identified as unscattered TM_1 mode, unscattered TM_2 mode, Bragg-scattered TM_1 mode, Bragg-scattered TM_2 mode, Bragg-scattered TE_2 mode, and Bragg-scattered TE_1 mode, respectively. The dashed line box in (a)–(e) indicates the bandgap caused by the interference of the modes (i) and (iii). The two dashed lines in (d) indicate the polar angle $\theta = 45°$ and $58.5°$.

square dashed box clearly indicates one of the bandgaps. As described previously, this bandgap is formed by the interference between scattered and unscattered TM_1 modes and occurs at the first Brillouin zone boundary. The central frequencies of this band gap for $\phi = 10°$, $20°$, $30°$, $40°$, and $50°$ are 0.496, 0.509, 0.532, 0.565, and $0.620 (\times 10^{15}$ Hz) respectively. The bandgap central frequency increases with increasing ϕ. Furthermore, examination of figure 6(e) reveals that there is clear coupling to the lower branch of this band gap up to about 0.614×10^{15} Hz. Comparing this with figure 4(a), it is apparent that this value exceeds the position of the upper band edge for $\phi = 0°$, which is positioned at approximately 0.495×10^{15} Hz. In other words, the rise in frequency of the centre of the bandgap from $\phi = 0°$ to $\phi = 50°$ is greater than the overall gap width at $\phi = 0°$. This clearly demonstrates that this bandgap is not 2D. At $\phi = 30°$ and $40°$, a second bandgap is clearly visible at the first Brillouin zone boundary, as shown in figures 6(c) and (d). This bandgap is caused by the interference of the unscattered TM_2 mode (ii) and the scattered TM_2 mode (iv). This bandgap is also not a complete 2D bandgap.

Figure 6 also shows the mode-crossings between Bragg-scattered modes and unscattered TM modes when polarisation conversion is present. Figures 6(c) and (d) clearly show that the scattered TE_2 mode (v) crosses with the TM_1 mode (i) at in-plane wavevector values of $2k_{xz}/k_g = 1.38$ and 1.6 with $\phi = 30°$ and $40°$, respectively. At these crossings there is an energy gap which is similar to the band-gap at the Brillouin zone boundary. As the azimuthal angle is increased the scattered TE_2 mode (v) increases in frequency and becomes flatter. Hence, the position of the mode crossing will rise in both frequency and in-plane wavevector. Beyond $\phi \sim 40°$ this crossing has moved outside the range accessible through silica prism coupling.

The scattered TE_2 mode (v) also interferes with the unscattered TM_2 mode (ii). This crossing is readily observed in figures 6(d) and (e). As for the first crossing discussed above it shifts its frequency and in-plane wavevector with an increasing azimuthal angle. In addition to the crossings caused by the scattered TE_2 mode, a further similar crossing is visible. This crossing is from the interference between the scattered TE_1 mode (vi) and the unscattered TM_1 mode, which appears in figures 6(d) and (e). Again, these crossings have the same behaviour as discussed above. In figures 6(e)–(g), crossings between the scattered TM_1 mode (iii) and the unscattered TM_2 mode are also observed.

To understand these modes better, the optical magnetic field distribution is computed, as shown in figures 7 and 8, for an azimuthal angle of $\phi = 40°$ and at each resonant frequency for polar angles of $\theta = 58.5°$ and $45°$. Note from figure 6(d) that the first two modes at $\theta = 58.5°$ are around the mode-crossing of the Bragg-scattered TE_1 mode and the unscattered TM_1 mode. Figure 7(a) shows the magnetic field distribution for the lower branch of the crossing, and figure 7(b) shows the field distribution for the upper branch. Relative to the corrugation, the field amplitude maxima near to the grating are observed in the troughs in both figures 7(a) and (b). However, the field maxima close to the silver/resist interface align with the troughs in figure 7(a) but align with the peaks in (b). This of course leads to the energy gap at the crossing. Figures 7(c)–(e) shows the field distribution for scattered TM_1 mode (the third mode at $\theta = 58.5°$), the scattered TE_2 mode (the fourth mode at $\theta = 58.5°$), and the scattered TM_2 mode (the fifth mode at $\theta = 58.5°$), respectively. It is straightforward to determine the order of these modes by counting the number of optical field minima per period. There is one optical field minimum per period in figure 7(c) and two minima per period in figure 7(d) and (e). Hence, they are the first-order and second-order modes, respectively.

The field distribution shown in figure 8(a) is for the unscattered TM_1 mode. It is difficult to tell clearly the position of the maxima, one can only see a continuous field minimum in the
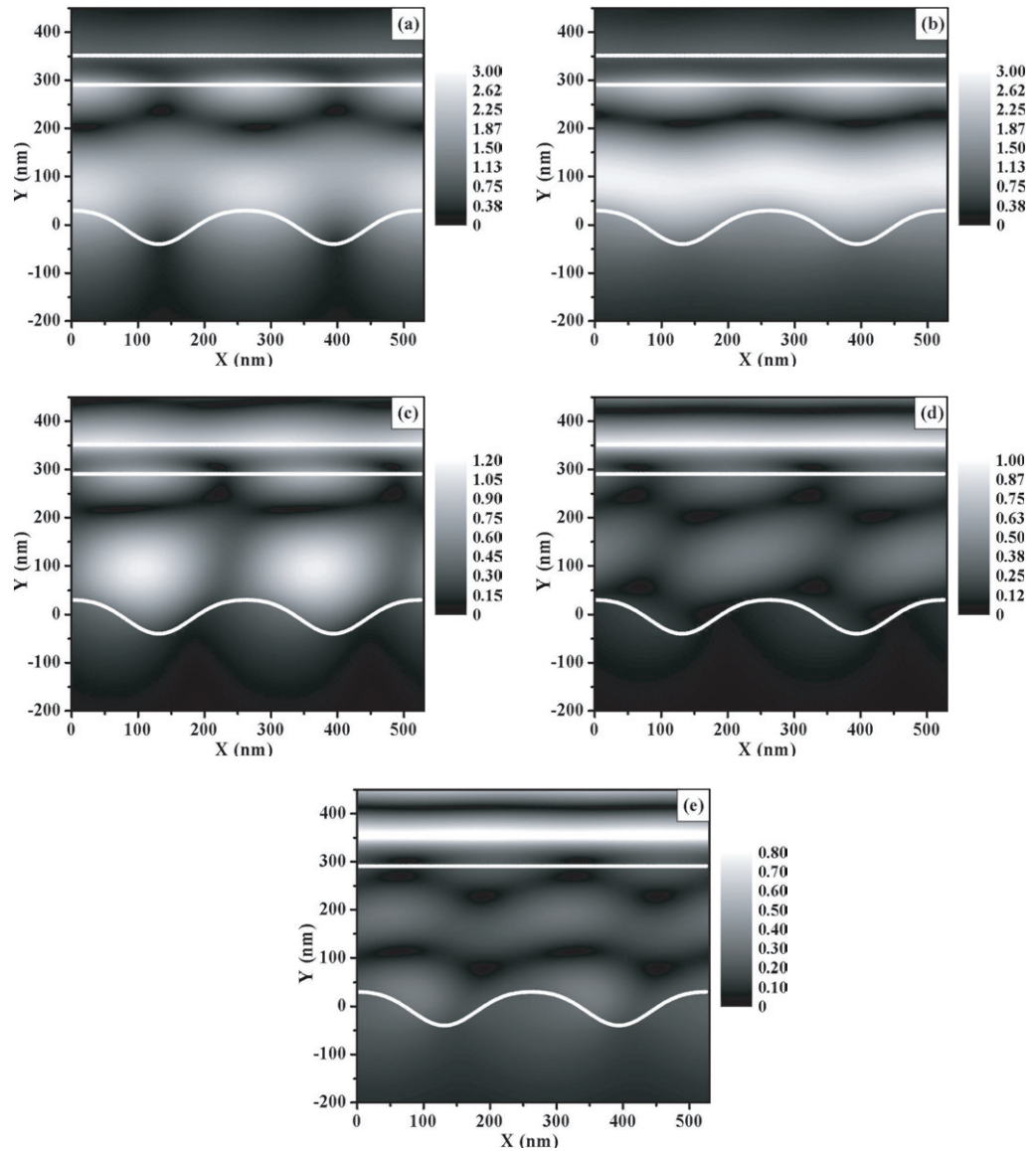
Figure 7. The magnitude field amplitude distribution for the guided modes resonance at polar angle $\theta = 58.5°$ and azimuthal angle $\phi = 40°$ for (a) $f = 0.522 \times 10^{15}$ Hz, (b) $f = 0.532 \times 10^{15}$ Hz, (c) $f = 0.571 \times 10^{15}$ Hz, (d) $f = 0.635 \times 10^{15}$ Hz and (e) $f = 0.709 \times 10^{15}$ Hz. The white line represents the waveguide structure.

resist waveguide medium. From figure 6(d), one sees that the second mode at $\theta = 45°$ is the same as the third mode at $\theta = 58.5°$. Both of them belong to the Bragg-scattered TM_1 mode. Comparing figure 8(b) with figure 7(c), the field distributions are almost the same except for the field intensity. The third mode at $\theta = 45°$ is around the mode-crossing of the scattered TE_2 mode and the unscattered TM_2 mode. The field distributions in figure 8(c) clearly show the interference of these modes. The field maximum occurring in the centre of the resist medium is now surrounded by four field minima. Figure 8(d) shows the magnetic field distribution for
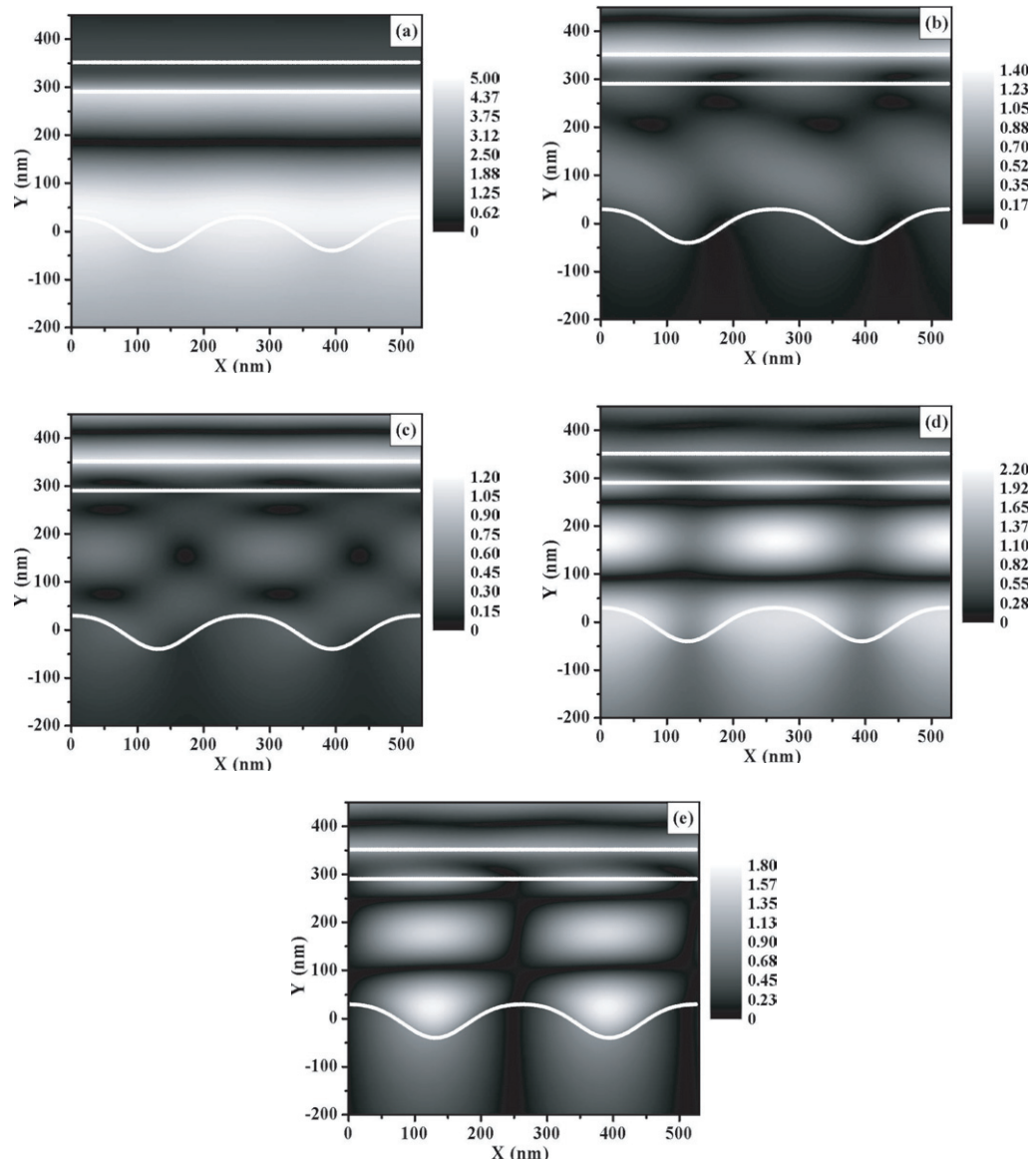
Figure 8. The magnitude field amplitude distribution for the guided modes resonance at polar angle $\theta = 45°$ and azimuthal angle $\phi = 40°$ for (a) $f = 0.394 \times 10^{15}$ Hz, (b) $f = 0.585 \times 10^{15}$ Hz, (c) $f = 0.643 \times 10^{15}$ Hz, (d) $f = 0.682 \times 10^{15}$ Hz and (e) $f = 0.729 \times 10^{15}$ Hz. The white line represents the waveguide structure.

the lower branch at the band gap where the scattered and unscattered TM_2 modes cross, and figure 8(e) shows the field distribution for the upper branch of this band gap. The obvious two field minima per period in both figures 8(d) and (e) demonstrate that these modes are second-order modes. In figure 8(d), the maxima are observed to align with the troughs of the resist grating in contrast with figure 8(e), in which the maxima are observed to align with the peaks. From figure 6(d), one sees that the last two modes at $\theta = 45°$ are much closer to the first Brillouin-zone boundary ($2k_{xz}/k_g = 1.305$) and belong to the different branch of the

IOP Institute of Physics Φ DEUTSCHE PHYSIKALISCHE GESELLSCHAFT

counterpropagating waveguide modes, respectively. For counterpropagating waveguide modes that cross at the first Brillouin-zone boundary standing waves are expected which consist of two eigensolutions. The antinodes of the magnetic field of one solution are positioned under troughs of the corrugation (as shown in figure 8(d)), whereas for the second solution they are positioned under the peaks (as shown in figure 8(e)). The asymmetry of the waveguide structure causes an energy difference between the two solutions, leading to a bandgap.

4. Conclusions

The optical properties of a short-pitch periodically corrugated photoresist waveguide structure on a thin silver tunnel barrier have been explored at $10°$ steps over the azimuthal angle range $\phi = 0°$–$90°$. Reflectivities at each ϕ for five different incident angles ($\theta = 45°, 48.4°, 51.8°, 55.2°$ and $58.5°$) have been measured and mapped onto the theoretical plots. Experimental data show excellent agreement with the model calculations. By comparing the predicted band structure with both TM and TE reflectivities all the modes supported by the structure are identified. Both experimental data and theoretical fitting show that the introduction of the corrugation into the waveguide introduces bandgaps in the dispersion of the guided modes. These band gaps raise their central frequencies with increasing azimuthal angle ϕ. By comparing the central frequency of bandgaps at different azimuthal angles, the nature of the bandgap that is not 2D has been demonstrated. In addition, when the azimuthal angle $\phi \neq 0°$ or $90°$ polarisation conversion leads to bandgaps where different types of modes cross. To understand the character of each of the modes, the optical magnetic field distributions at azimuthal angle $\phi = 40°$ at each resonant frequency for polar angles of $\theta = 58.5°$ and $45°$ are explored. The field distributions help to distinguish the order of the modes and demonstrates the cause of the energy splitting at the mode-crossing.

In the context of emissive devices the presence of the bandgap can inhibit the emission if the emission frequency lies in the gap. Both types of bandgaps caused by the modes self-crossing at the Brillouin zone boundary and by different modes anticrossing at a point other than the Brillouin zone boundary can play an important role in controlling the emission in waveguide structures.

Acknowledgment

References

[1] Fano U 1941 *J. Opt. Soc. Am.* **31** 213
[2] Weber W H and McCarthy S L 1975 *Phys. Rev.* B **12** 5643
[3] Nash D J and Sambles J R 1998 *J. Mod. Opt.* **45** 2585
[4] Chang R K and Furtak T E (eds) 1982 *Surface Enhanced Raman Scattering* (New York: Plenum)
[5] Garcia-Vidal F J and Pendry J B 1996 *Phys. Rev. Lett.* **77** 1163
[6] Homola J, Yee S S and Gauglitz G 1999 *Sensors Actuators* (*Chemical*) B **54** 3
[7] Ebbesen T W, Lezec H J, Ghaemi H F, Thio T and Wolff P A 1998 *Nature* **391** 667
[8] Quinten M, Leitner A, Krenn J R and Aussenegg F R 1998 *Opt. Lett.* **23** 1331

IOP Institute of Physics   Φ DEUTSCHE PHYSIKALISCHE GESELLSCHAFT

[9] Ozbay E 2006 *Science* **311** 189

[10] Bozhevolnyi S I, Volkov V S, Devaux E, Laluet J-Y and Ebbesen T W 2006 *Nature* **440** 508

[11] Hornauer D and Raether H 1973 *Opt. Commun.* **7** 297

[12] Raether H 1988 *Surface Plasmons* (Berlin: Springer)

[13] Müller K G, Veith M, Mittler-Neher S and Knoll W 1997 *J. Appl. Phys.* **82** 4172

[14] Hibbins A P and Sambles J R 2000 *Phys. Rev.* E **61** 5900

[15] Hibbins A P and Sambles J R 2000 *J. Appl. Phys.* **87** 2677

[16] Salakhutdinov I F, Sychugov V A and Parriaux O 1998 *Quantum Electron.* **28** 983

[17] Park S, Lee G, Song S H, Oh C H and Kim P S 2003 *Opt. Lett.* **28** 1870

[18] Salt M G and Barnes W L 1999 *Opt. Commun.* **166** 151

[19] Salt M G, Andrew P and Barnes W L 2001 *J. Opt. Soc. Am.* B **18** 240

[20] Barnes W L 1999 *J. Lightwave Technol.* **17** 2170

[21] Dowling J P, Scalora M, Bloemer M J and Bowden C M 1994 *J. Appl. Phys.* **75** 1896

[22] Chandezon J, Dupuis M T, Cornet G and Maystre D 1982 *J. Opt. Soc. Am.* **72** 839